Mesoscopic analyses of the draping of 3D woven composite reinforcements based on macroscopic simulations

Jie Wang, Peng Wang, Nahiene Hamila, Philippe Boisse

Version of Record: https://www.sciencedirect.com/science/article/pii/S0263822320311314
Manuscript_9806647b56f986ca515820f98cbf67b0

Mesoscopic analyses of the draping of 3D woven composite reinforcements based on macroscopic simulations

Jie Wang[a], Peng Wang[b], Nahiene Hamila[a], Philippe Boisse[a*]

[a] *Université de Lyon, LaMCoS CNRS, INSA-Lyon, F-69621, France*

[b] *Université de Haute-Alsace LPMT, ENSISA, Mulhouse, F-68000, France*

Abstract:

Mesoscopic analyses of textile composite reinforcements consider each yarn as a deformable solid in contact with its neighbours. They provide the internal architecture of the deformed woven fabric that conditions the permeability of the reinforcement and the mechanical characteristics of the cured woven composite. With regard to preform draping, simulations are generally carried out on a macroscopic scale because mesoscopic analyses of the forming process have a computational cost which is prohibitive. This paper proposes a meso-macro analysis of the forming of textile reinforcements in which an embedded mesocopic geometry is first deduced from the macroscopic simulation of the draping. This solution can lead to excessive yarn extensions. Local mesoscopic simulations based on the embedded analysis and restricted to a limited area, overcome this inconvenience. This mesoscopic approach requires a computational cost that is reasonable.

Keywords: Meso-macro analyses, Forming, Hyperelasticity, 3D textile reinforcement, RVE.

1. Introduction

The analysis and simulation of the draping of textile composite reinforcements has given rise to a great deal of research work over the past decades. Most approaches are carried out on a macroscopic scale and consider the woven fabric as a continuous medium [1,2]. The mechanical behaviour of this continuous medium must reflect the specificities textile reinforcement during draping. These macroscopic approaches can predict the global wrinkling of the woven fabric, which is the major defect that can occur during draping [3-6]. Nevertheless, some important phenomena take place on a smaller scale during the draping process. On a mesoscopic scale, the woven fabric is considered as a set of yarns in contact with their neighbours. Defects such as gaping (gap between two yarns) [7-10], local buckling of yarns [8,11,12] can be analyzed at the mesoscopic scale. Beyond the defects, the architecture of yarns on a mesoscopic scale makes it possible to calculate the permeability of the textile reinforcement by simulating a flow of resin in the fabric [13-17]. The mesoscopic analysis provides the direction and the volume fraction of the fibres in the yarns that conditions the mechanical properties of the cured

*Corresponding author.

E-mail address: philippe.boisse@insa-lyon.fr (P. Boisse).

composite [18-23]. Simulations of the entire preform draping using mesoscopic models have been developed [7,24-29]. These meso-models of the entire preform require very large computing power because of the high number of yarns and their contacts.

The objective of this paper is to propose a simulation approach on the mesoscopic scale with low numerical cost based on macroscopic simulation. Approach of the same nature have been proposed in a more general framework of solid mechanics [30-34] and for the analyses of composite structures [35]. In the present article, the embedded mesoscopic geometry is derived from the macroscopic deformation. This may be sufficient for some mesocopic scale analyses (e.g. permeability calculations). Nevertheless, as will be shown, it generally has drawbacks, in particular excessive yarn extensions. A local mesoscopic analysis avoids these problems. This local analysis is performed from the embedded mescopic geometry and only in areas where mesocopic simulation is required. As a result, the numerical cost is moderate. Two examples are presented: three-point bending and hemispherical forming of a 3D non crimp woven fabric. Experimental analyses, macroscopic, embedded mesoscopic and local mesoscopic simulations are presented and compared.

The mesoscopic analyses are performed locally as downstream simulations after the macroscopic analysis. The aim is to obtain a local solution on a mesoscopic scale. The accuracy of the macroscopic simulation is essential for the quality of the analyses.

After a macroscopic simulation, the presented mesoscopic analyses are done, in two steps. An embedded mesoscopic analysis (without mechanical resolution), then a local mesoscopic analysis which aims to avoid some of the defects of the previous calculation, in particular excessive extensions. The two mesoscopic steps can be considered as two approaches and the results compared.

2. Macroscopic simulation of the forming with a hyperelastic constitutive law

Because of possible slippage between constituting fibers and yarns, the mechanical behavior of textile reinforcements is very specific compared with traditional materials, such as metals. It leads to a strong tensile stiffness in the fiber directions in comparison to the other rigidities. In the case of thick textile reinforcement, 3D constitutive law is needed. To model the large deformations of these textile reinforcements, hyperelastic constitutive laws for orthotropic materials have been proposed [36-40]. In particular the model developed in [41] is adapted for the analysis of the deformation of 3D textile reinforcements. Nevertheless, when using this type of model, some discrepancies can be identified because of the limitation of the standard continuum mechanics of Cauchy framework in which these models are formulated. Such models are not able to simultaneously take into account the low transverse shear property (due to possible slippage between the fibres) and the local bending stiffness of the fibres [42]. Afterwards, Mathieu et al. [43] has improved the 3D hyperelastic model by taking into account the local curvature in 3D hexahedral finite elements. This approach has proven to be effective as shown by the comparison between simulations and experimental results. For the same objective, other models have been developed using second gradient approaches [44-46]. In this paper, the enhanced hyperelastic

model [43] is used to carry out the macroscopic simulations. The material parameters of this constitutive model are identified by different experiments using direct or inverse methods.

2.1 Studied textile reinforcement

The fabric analyzed in this paper is an E-glass 3D non-crimp orthogonal woven fabric (Fig.1). Tab.1 shows the geometric and physical characteristics of the woven reinforcement. The warp and weft yarns are not interlaced. The binder yarns are present through the thickness of the reinforcement. Thus, mechanical properties in the transverse direction are improved, particularly for the resistance to delamination. Fig.1 shows the structure of this 3D orthogonal woven reinforcement and its architecture obtained by X-ray tomography. This reinforcement is taken as an example to show the different steps of the proposed multi-scale method.

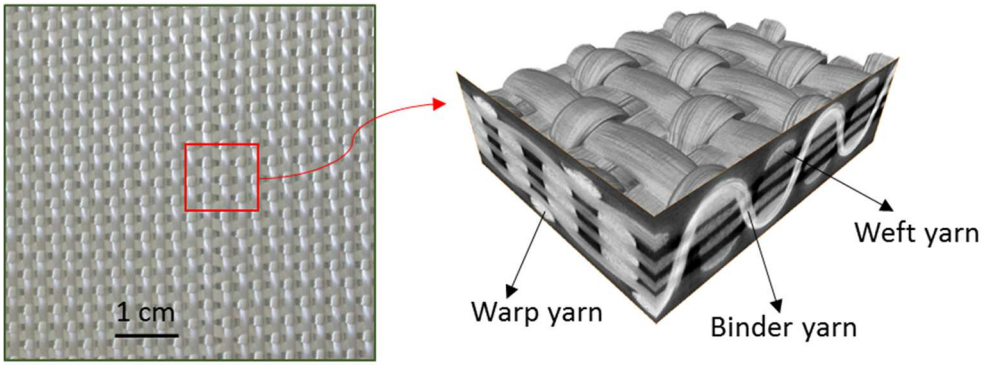

Fig.1 Structure of the 3D non-crimp orthogonal woven fabric and its 3D architecture by X-ray tomography

Tab.1 Geometric characteristics of the woven reinforcement [47]

Linear mass, ±6% (g/km)	Filament diameter (μm)	Rupture force (N)	Areal density (g/m^2)	Thickness of fabric (mm)	Number of fibers per yarn
900	15	121.9	2722	3.2	2000

2.2 Hyperelastic constitutive law for the 3D reinforcement

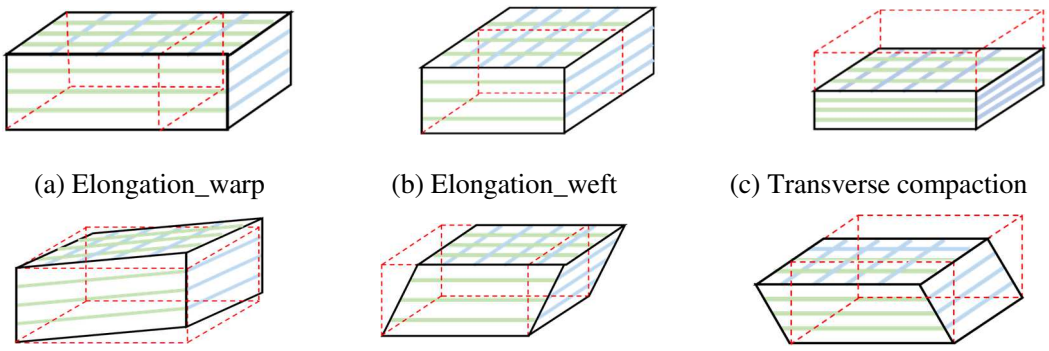

(a) Elongation_warp (b) Elongation_weft (c) Transverse compaction

(d) In-plane shear (e) Transverse shear_warp (f) Transverse shear_weft

Fig.2 Six deformation modes of a 3D woven reinforcement [41]

The considered hyperelastic constitutive law models the deformation of thick 3D composites reinforcements. Six deformation modes are considered (Fig.2). Thick textile reinforcements have three privileged directions: the warp direction $\underline{M}_1$; the weft direction $\underline{M}_2$ and the direction of thickness $\underline{M}_3$ that is perpendicular to the plane $(\underline{M}_1, \underline{M}_2)$. According to the representation theorems [48], the strain energy density function of an orthotropic material can be written as:

$$w^{orth} = w^{orth}\left(I_1, I_2, I_3, I_{41}, I_{42}, I_{43}, I_{412}, I_{423}, I_{51}, I_{52}, I_{53}\right) \tag{1}$$

where I_1, I_2, I_3 are the classical invariants of the right Cauchy-green tensor $\underline{\underline{C}} = \underline{\underline{F}}^T \underline{\underline{F}}$:

$$I_1 = Tr(\underline{\underline{C}}); \quad I_2 = \frac{1}{2}\left(Tr(\underline{\underline{C}})^2 - Tr(\underline{\underline{C}}^2)\right); \quad I_3 = Det(\underline{\underline{C}}) \tag{2}$$

and the mixed invariants are defined by the direction vectors $\underline{M}_i$ (i=1,3):

$$I_{4i} = \underline{M}_i \cdot \underline{\underline{C}} \cdot \underline{M}_i, \quad I_{4ij} = \underline{M}_i \cdot \underline{\underline{C}} \cdot \underline{M}_j \quad \text{and} \quad I_{5i} = \underline{M}_i \cdot \underline{\underline{C}}^2 \cdot \underline{M}_i \tag{3}$$

For each deformation mode of Fig. 2, a corresponding physical invariant is defined in Equation (4) by combination of the invariants defined in Equation (2) and (3) [41].

$$\begin{aligned} I_{elong\alpha} &= \ln(\sqrt{I_{4\alpha}}) \quad (\alpha = 1,2) & I_{comp} &= \frac{1}{2}\ln\left(\frac{I_3}{I_{41} I_{42}(1 - I_{cp}^2)}\right) \\ I_{cp} &= \frac{I_{412}}{\sqrt{I_{41} I_{42}}} = \sin(\gamma_{12}) & I_{ct\alpha} &= \frac{I_{4i3}}{\sqrt{I_{4\alpha} I_{43}}} = \sin(\gamma_{\alpha 3}) \end{aligned} \tag{4}$$

$I_{elong\alpha}(\alpha = 1,2)$ are the stretch invariants in warp and weft directions; I_{comp} is the compression invariant in the thickness direction; I_{cp} is the in-plane shear invariant and $I_{ct\alpha}$ are the transverse shear invariants in warp and weft directions. In this hyperelastic model, a strain energy potential is a function of the right Cauchy Green physical invariants. Although couplings between the different properties have been shown [49-51], it is assumed, for the purpose of simplicity, that the contribution to the strain energy potential of each deformation mode is independent from the others. Therefore, the strain energy density is the sum of 6 terms:

$$w = w_{elong1}(I_{elong1}) + w_{elong2}(I_{elong2}) + w_{comp}(I_{comp}) + w_{cp}(I_{cp}) + w_{ct1}(I_{ct1}) + w_{ct2}(I_{ct2}) \tag{5}$$

The form of each strain energy density can be written in polynomial form [43]:

$$w = \begin{cases} \sum_{i=1}^{6} k_i I^i & \text{if } I > 0 \\ \sum_{i=1}^{6} k_{i+6} I^i & \text{if } I \le 0 \end{cases} \tag{6}$$

where I is the physical invariant related to the concerning strain energy. The coefficients k_i need to be determined by appropriate experiments. Then, the second Piola-Kirchhoff stress tensor $\underline{\underline{S}}$ and Cauchy stress tensor $\underline{\underline{\sigma}}$ can be calculated by derivation:

$$\underline{\underline{S}} = 2\frac{\partial w}{\partial \underline{\underline{C}}} = 2\frac{\partial w_k}{\partial I_k}\frac{\partial I_k}{\partial \underline{\underline{C}}} \tag{7}$$

$$\underline{\underline{\sigma}} = J^{-1}\underline{\underline{F}}\cdot\underline{\underline{S}}\cdot\underline{\underline{F}}^T = \frac{2}{J}\underline{\underline{F}}\cdot\frac{\partial w}{\partial \underline{\underline{C}}}\cdot\underline{\underline{F}}^T \tag{8}$$

2.3 Taking into account the curvature of the fibers

The presented anisotropic hyperelastic model used in hexahedral finite element is based on the standard continuum mechanics of Cauchy. It has been shown that beyond this approach, the fiber bending stiffness associated to the curvature is significant to depict correctly the mechanical behavior of fabrics [42, 43]. An independent bending stiffness of fibers has been added into the 3D hexahedral finite element [43]. The curvature in the hexahedral element is calculated from the geometrical position of neighboring elements (Fig.3) [52]. Then, a nonlinear constitutive law is defined by Equation (9) and this fiber bending stiffness is added to the others. M_{bend} is the bending moment, χ is the curvature and D_0 and D_1 are parameters determined by inverse identification:

$$M_{bend} = \begin{cases} \left(D_0 - D_1|\chi|\right)\chi & \text{if } \chi < \dfrac{D_0}{2D_1} \\ \dfrac{D_0}{2}\chi & \text{if not} \end{cases} \tag{9}$$

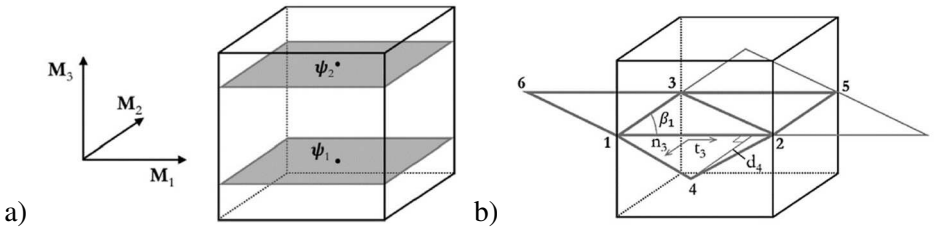

Fig.3 a) Integration areas in the hexahedral element
b) Computation of curvatures from neighbouring elements [43]

2.4 Identifications of material parameters

The identification of material parameters k_i of Eq. (6) were carried out by the following tests: tensile tests in the warp and weft directions, transverse compaction test, in-plane shear test, and transverse shear tests. In addition, the two parameters D_0 and D_1 were determined by a bending test.

The main interest of the physical invariants used in the strain energy densities (Eq. (5)) is that they correspond to the deformations of the elementary tests and make possible a simple identification of the potentials, and thus of the k_i of equation (6). Each test contributes to a specific energy density.

These tests are briefly described below and the identified parameters are given in Tab.A1 in *Appendix A*.

2.4.1 Elongations in warp and weft directions

Textile materials have a high stiffness in tension with respect to other stiffnesses. This results in small tensile strains in the yarns (a few percent before rupture). The hyperelastic tensile potential parameters are given in Tab. A1 in the case of the studied textile reinforcement.

2.4.2 Transverse compaction

This behavior is analyzed by a compaction test. The device with two circular plates of 120 mm is shown in Fig.4 a). The specimen is a 120 mm × 120 mm fabric. As the compaction displacement increases, the fiber volume ratio increases and the stiffness gradually increases until it reaches high values. From the experimental force/displacement curve, the parameters of the hyperelastic transverse compaction potential are identified.

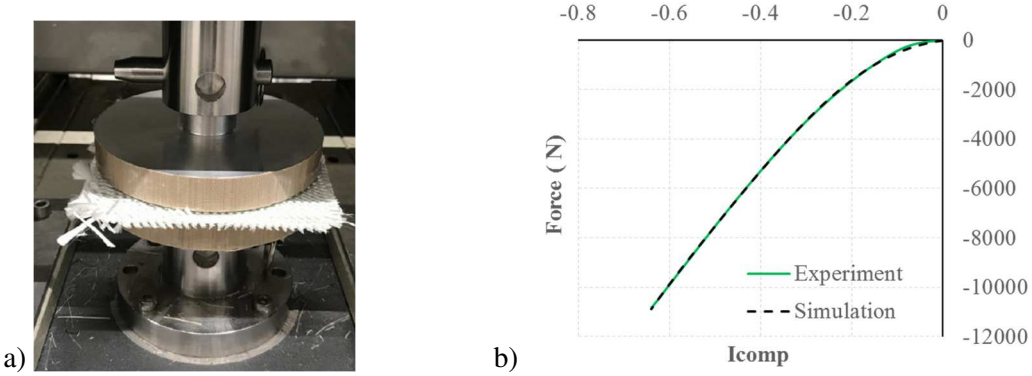

Fig.4 a) Experimental device and b) experimental and numerical identification curves

2.4.3 In-plane shear

The Bias Extension Test (BET) is used to realize the identification of material parameters of in-plane shear mode [53-56]. In order to obtain an in-plane shear deformation, the yarns of a specimen with dimensions 210×70 mm are oriented at 45° with respect to the direction of traction.

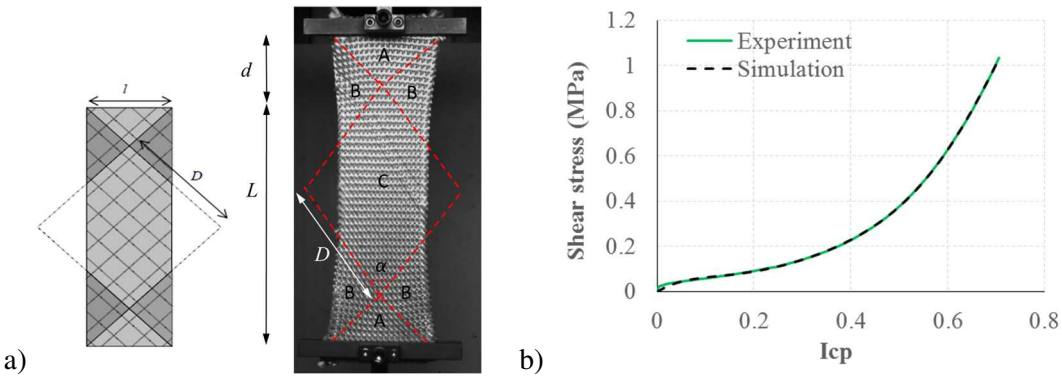

Fig.5 a) Specimen in Bias Extension Test and b) experimental and numerical identification curves

2.4.4 Transverse shear

The specimen with dimensions of 70 × 20 mm^2 is fixed on the jaw surfaces (Fig.6). This studied reinforcement is not balanced and the transverse shear behaviour in the direction warp and weft is different and transverse shear potentials are identified in the warp and weft directions.

2.4.5 Additional bending behaviour of fibres

The aim here is to complete the 3D hyperelastic behaviour with an additional stiffness linked to the curvature of the fibres [43]. A three-point bending test is carried out for this identification analysis. A Levenberg-Marquardt algorithm is used for an inverse identification of the coefficients D_0 and D_1 of Equation (9).

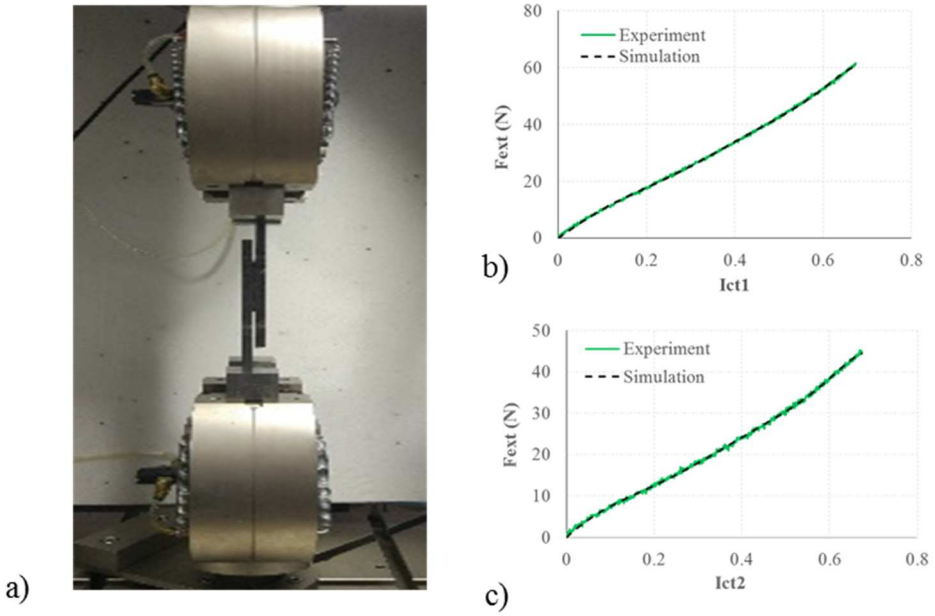

Fig. 6 a) Experimental device and identification curves for transverse shear in the b) warp and c) weft directions

2.5 Macroscopic textile reinforcement forming simulations

The macroscopic simulations (i.e. the simulations at the scale of the textile preform) carried out in this paper use the in-house software PlasFib [57-59]. This finite element code uses an explicit dynamic scheme as is the case with most software for forming simulation. Macroscopic simulations of three points bending and hemispherical stamping of are carried out using the above hyperelastic behavior and the parameters identified for the 3D non-crimp orthogonal woven fabric. The macroscopic results serve as a basis for mesoscopic modelling in the macro-meso method developed.

2.5.1 Three point bending

A 200×30 mm^2 strip of 3D non-crimp woven fabric is loaded in three point bending with a 30 mm deflection imposed at a speed of 10 mm/min (Fig.7).

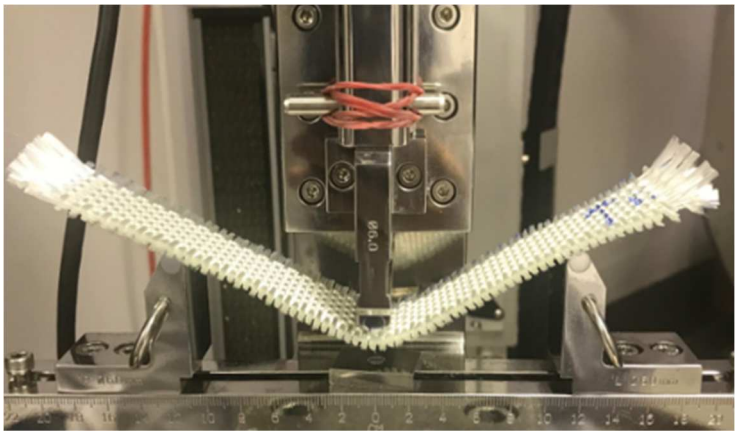

Fig. 7 Three points bending

The paper focuses on the bending in the warp direction with which the binder yarns are aligned (Fig.8). Fig. 9 shows the comparison of the deformed middle line obtained by simulation and experiment. They are in correct agreement.

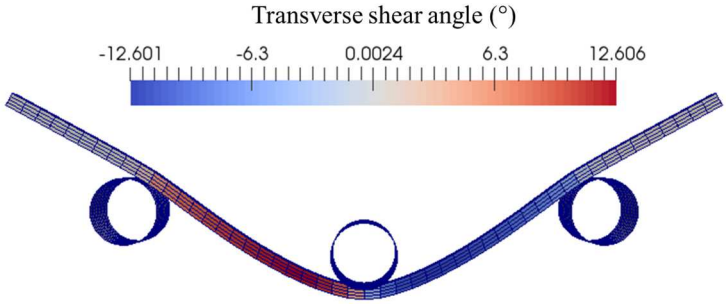

Fig. 8 Transverse shear angle of the initial and deformed preform in bending

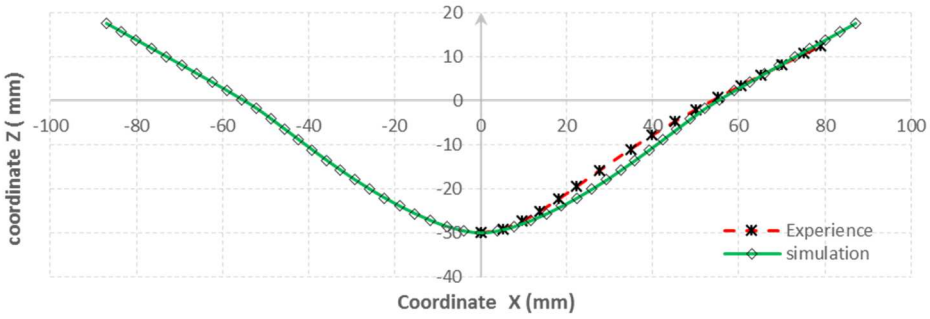

Fig. 9 Comparison of experimental and simulated middle lines of the preform

2.5.2 Hemispherical stamping

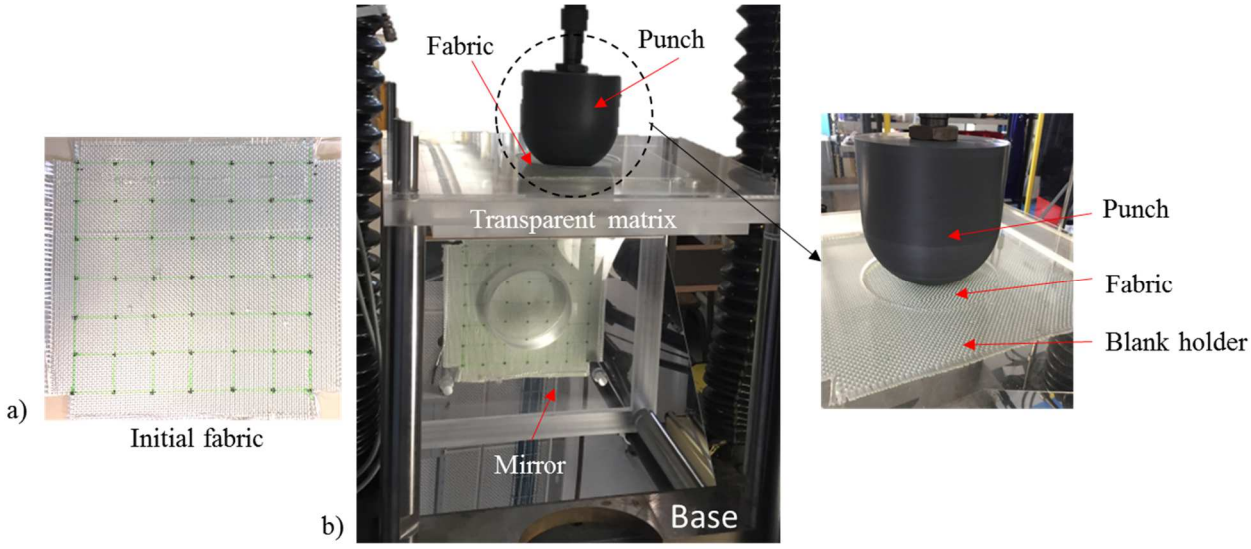

Fig.10 a) Initial fabric and b) Experimental device for hemispherical stamping

As shown in Fig.10a, green lines and black dots are drawn on the yarns crossings to follow the evolution of the in-plane shear angle. The experimental device is used to stamp a preform whose initial dimensions are 290×290 mm^2. When the reinforcement is placed on the die that is fixed and transparent, the mirror below shows the deformation of the textile reinforcement. Because the punch is double curved, the final shape is obtained mainly by in-plane shear strains A transparent blank holder is used to add tension that avoids possible wrinkles. The diameter of the punch is 150 mm.

Fig.11 display the final deformed geometry of the textile preform obtained through experiment and simulation. The in-plane shear angles can then be measured with the help of the lines drawn on the fabric blank. The in-plane shear angles measured in the experiments and obtained by simulation are close.

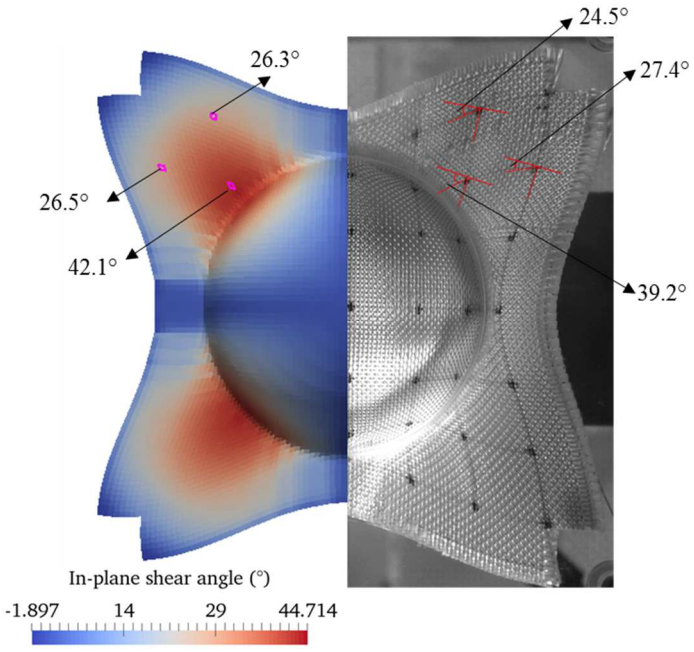

Fig.11 Top view of the deformed preform: simulation (left) and experiment (right)

3. Mesoscopic analyses based on macroscopic simulations (embedded mesoscopic geometries)

Mesoscopic analyses consider the deformation of each yarn in contact with their neighbours.. Analyses of the entire preform at the mesoscopic scale have been carried out [7,24-29], but the size of the numerical model and the computation time are very important. In this paper, with the aim of analyzing mesoscopic deformations of the woven reinforcement during the forming process, the developed macro-meso method proposes to carry out mesoscopic analyses by using, as a first step, the information obtained at the macroscopic scale. If macroscopic information is pertinent, it should be able to provide certain basic elements at the mesoscopic scale. In a first step, the embedded mesoscopic geometry is determined from the macroscopic simulation.

3.1 Mesoscopic geometry of the undeformed RVE

In this work the 3D textile reinforcement in its initial configuration is considered to be periodic. In a mesoscopic modelling, the *Representative Volume Element* (RVE) is the smallest elementary pattern, which allows reconstituting the entire fabric by repetitions and translations [60]. The geometry of the RVE of the 3D non-crimp woven fabric studied in the present paper is obtained using X-ray micro tomography (Fig. 12) [61]. A mesh composed of prismatic elements is generated from this geometry. The finite element model constructed has no interpenetrations as can occur using software packages for 3D modelling of textiles [62].

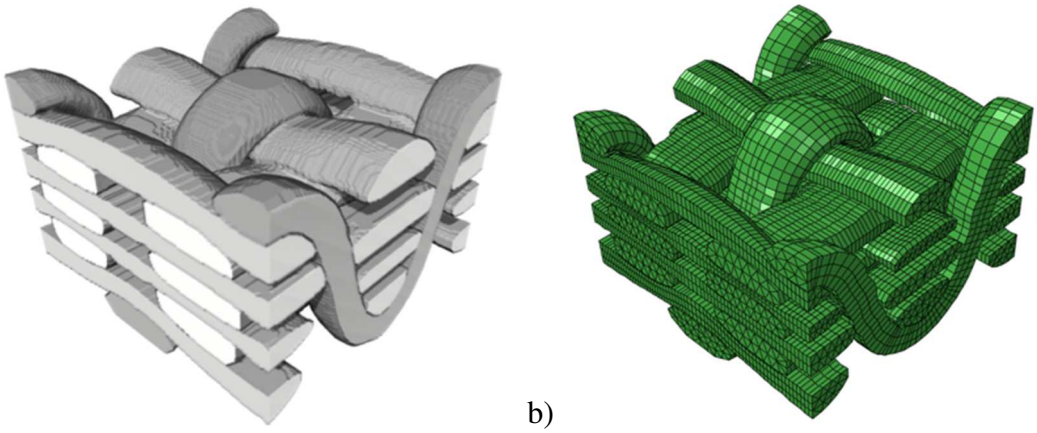

Fig.12 a) Geometry obtained by X-ray tomography of the 3D non-crimp woven reinforcement, b)-Corresponding prism mesh

To obtain a first mesoscopic model, the woven elementary cells (RVE) embedded in the macroscopic reinforcement are considered. The initial configuration of the RVE is given by the X-ray tomography analysis and the associated mesh (Fig. 13).

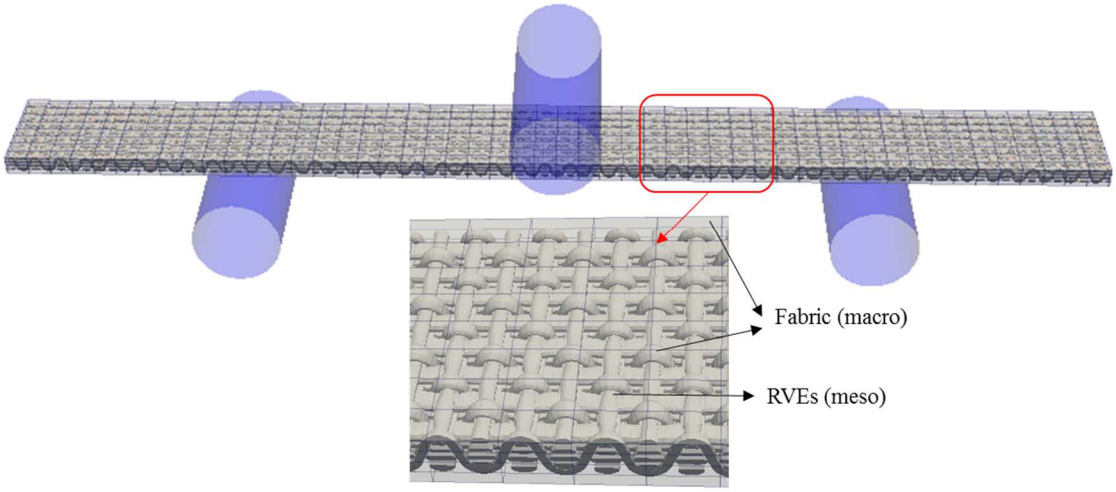

Fig.13 Initial state: mesoscopic RVEs embedded in a macroscopic mesh of the fabric

3.2 Deformed geometry of the embedded mesoscopic model

Each node of the mesoscopic model can be located (embedded) in a macroscopic element (Fig.14). An embedded mesoscopic element is deformed together with the macroscopic element and its nodes have constant coordinates in the macroscopic reference element.

$$\underline{X_{meso}}(\xi,\eta,\zeta) = \sum_{i=1}^{8} \underline{N_i}(\xi,\eta,\zeta)\ \underline{X^i_{macro}}(x,y,z) \tag{10}$$

where ξ, η, ζ are the reference coordinates in the macro element, $\underline{X_{meso}}$ and $\underline{X_{macro}}$ the spatial coordinates of the mesoscopic and macroscopic node.

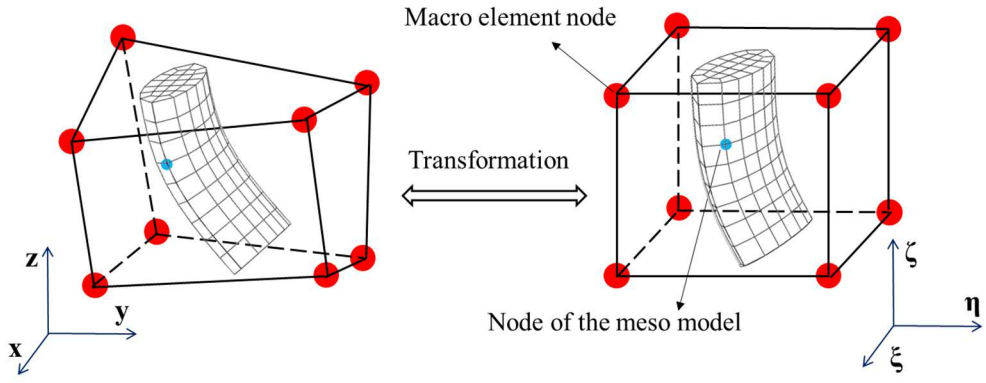

Fig.14 Embedded meso model in a macro element. Real and reference frames.

In the initial and deformed configuration, the naturel coordinates (ξ, η, ζ) of a mesoscopic node in the corresponding macroscopic element remain constant and the position of a mesoscopic embedded element remains constant within the macroscopic element. Consequently, the deformation obtained by the macroscopic simulation can provide a first deformed geometry of the RVEs at the mesoscopic scale in the deformed configuration that is called embedded meso model.

3.3 Analysis of deformations on a mesoscopic scale

To analyze the deformations of the meso-FE model, strain invariants corresponding to deformation modes at the mesoscopic scale are calculated from the initial and deformed geometries of the yarns (Fig.15).

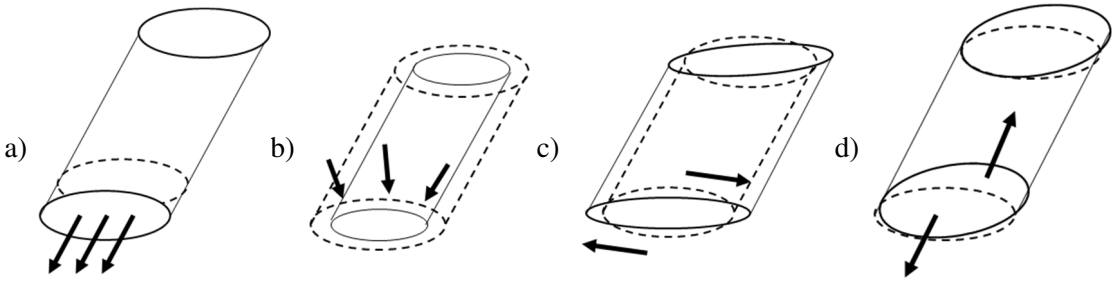

Fig.15 Deformation modes of a yarn: (a) elongation (b) compaction (c) distortion (d) longitudinal shear

The yarns are assumed to be transversely isotropic. For this type of material, a hyperelastic strain energy potential in the following form can be defined [48]:

$$w = w(\underline{\underline{C}}, \underline{M}) = w(I_1, I_2, I_3, II_4, II_5) \tag{11}$$

where I_1, I_2, I_3 are classic invariants defined in Equation (2), and II_4, II_5 are mixed invariants defined by the direction of the fibers $\underline{M}$:

$$II_4 = \underline{M} \cdot \underline{\underline{C}} \cdot \underline{M} \qquad II_5 = \underline{M} \cdot \underline{\underline{C}}^2 \cdot \underline{M} \tag{12}$$

The physical invariants that correspond to the deformation modes are introduced [67] (Fig.15). They are linked to the above invariants and are used to quantify the deformation at the mesoscopic scale.

$$I_{elong} = \frac{1}{2}\ln\sqrt{I_4} \qquad I_{comp} = \frac{1}{4}\ln\frac{I_3}{I_4}$$
$$I_{dis} = \frac{1}{2}\ln\left(\frac{I_1 I_4 - I_5}{2\sqrt{I_3 I_4}} + \sqrt{\left(\frac{I_1 I_4 - I_5}{2\sqrt{I_3 I_4}}\right)^2 - 1}\right) \qquad I_{sh} = \sqrt{\frac{I_5}{I_4^2} - 1} \tag{13}$$

where I_{elong} is the stretch invariant in the fiber direction; I_{comp} is the transverse compression invariant; I_{dis} is the transverse distortion invariant and I_{sh} is the longitudinal shear invariants of the yarn.

3.4 Embedded mesoscopic analyses: three points bending

The geometry of the reinforcement at mesocopic scale (Fig. 12), positioned in the undeformed (flat) configuration of the bending specimen defines the embedded mescoscopic elements (Fig. 16a). They are fixed in the macroscopic model and follow it in its deformation (Fig. 16b and 17). From the macroscopic simulation presented in section 2.5.1, the embedded mesoscopic analysis of three points bending provides the deformations of the yarns, their final orientations and then the voids in the unit

cell. These results can be used for the calculation of permeability in the following resin injection stage. Fig.16 presents the initial and deformed geometries of the textile reinforcement in three point bending. Fig.17 displays the mesoscopic elongation and transverse compaction invariants of yarns in the bending test.

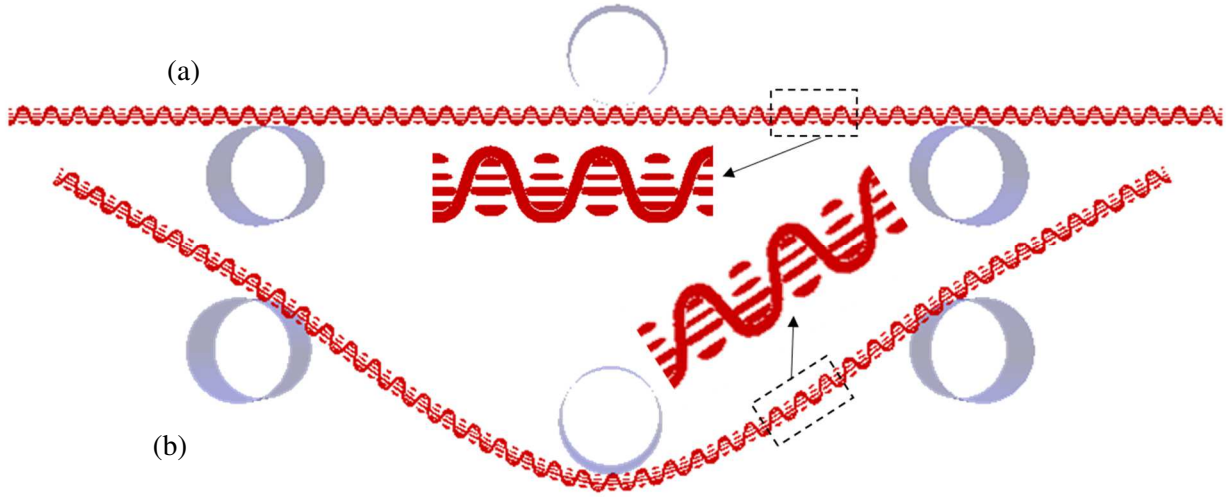

Fig.16. Three point bending: Transverse sections of the initial (a) and deformed (b) geometries

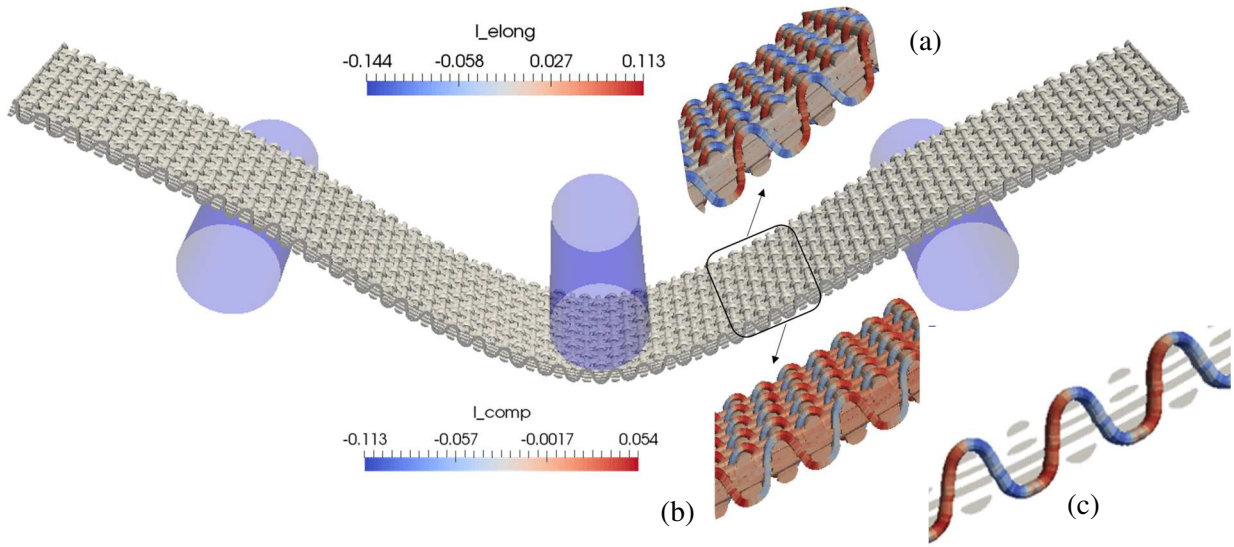

Fig.17. Three point bending: Mesoscopic deformation invariants:
(a) elongation, (b) compaction and (c) elongation in the binder yarn.

3.5 Embedded mesoscopic analyses: hemispherical stamping

This embedded mesoscopic analysis is based on the macroscopic simulation of the hemispherical forming presented in section 2.5.2. The mesoscopic embedded elements are defined from the mesoscopic geometry of the reinforcement (Fig. 12) positioned in the initial macroscopic reinforcement. These mesoscopic embedded mesoscopic elements deform with the macroscopic model. The embedded mesoscopic analysis of the hemispherical stamping provides the orientations and deformation of each

yarn (Fig.18). This deformed preform with a double curved shape can be achieved thanks to in-plane shear.

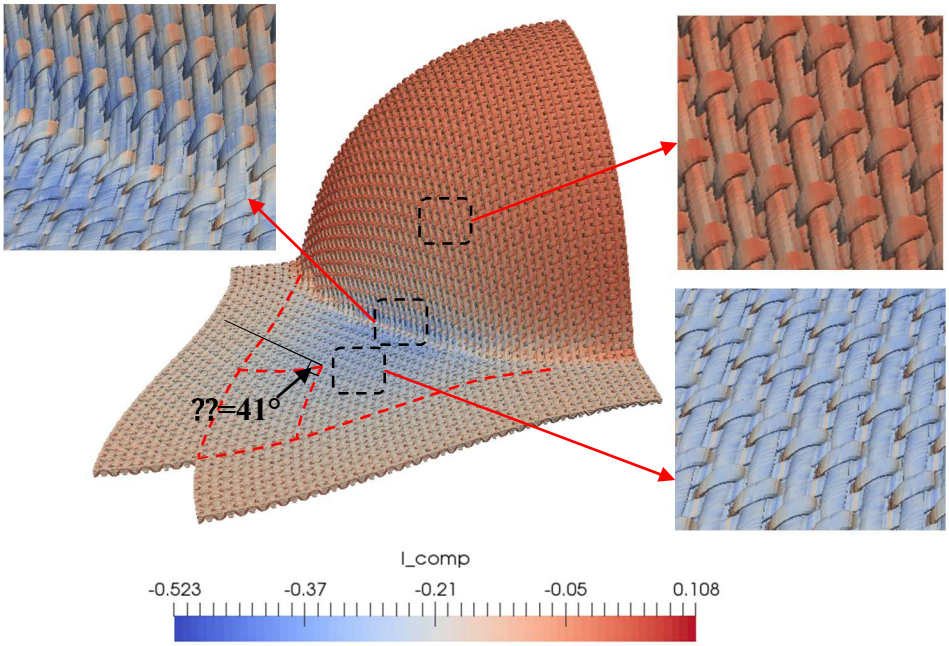

Fig. 18. Hemispherical forming. Embedded mesoscopic analysis.

Deformations of yarns in compaction (Invariant Icomp).

4. Local mesoscopic simulations from the embedded analyses

The macro-meso embedded analysis described in section 3 can provide a solution at the mesoscopic scale in forming analysis. It is very fast and may be enough to determine some quantities such as permeability. However, the equations of mechanics at the mesoscopic scale are not strictly verified. The deformed mesocopic embedded configuration is not obtained by solving a mechanical problem but is directly deduced from the macroscopic analysis, itself approximated given the assumptions on the continuous medium and the finite element approach. The embedded mesoscopic analysis provides displacements and deformations in the yarns. Given the constitutive law, the stresses do not check the local equilibrium. In particular, this approach can lead to excessive elongations of yarns because it does not take into account the local slippage between the yarns. This point is first highlighted. To overcome this difficulty, a local mesoscopic simulation based on the macroscopic analysis and the embedded mesoscopic analysis is proposed. Finally, the mesoscopic numerical results are compared with the experiment.

4.1 Excessive elongations

In the results obtained by the macro-meso embedded analysis, some excessive elongation may occur. For instance in Fig. 17c, the elongations of the binder yarn reach 11%, which is excessive. This

is because the approach is based on the macroscopic analysis and does not take into account the local slippage between the yarns.

Fig. 19 considers the case of a shear deformation of a macroscopic finite element. This deformation is frequent in the forming of textile materials. The two blue lines represent two yarns in the undeformed macroscopic element. Besides, the two red lines represent the same two yarns in the deformed macroscopic element. In this element, the diagonals M_{diag1} and M_{diag2} have the maximum variations in length during shear deformation. The elongation is zero for yarns oriented by the sides of the element. For intermediate yarns such as those considered in Fig. 19, the elongation is important and much larger than effective stretching of yarns in the fabric. In particular, the elongations of the binder yarns are large (Fig.17c).

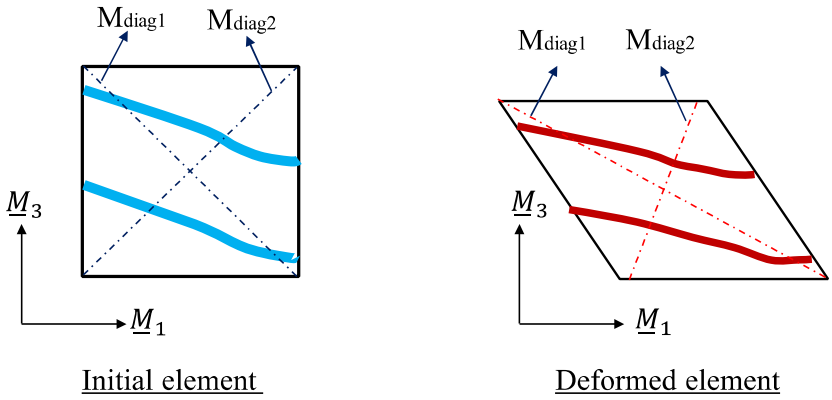

Fig.19. Elongation of yarns in a sheared macroscopic element

4.2 Local mesoscopic simulation

The macro-meso embedded analysis avoids having to carry out a mesoscopic scale simulation for the entire textile reinforcement that is numerically very expensive and it is not always possible to carry out. In order to use this method and avoid the spurious yarn elongations highlighted in the previous section, a mesoscopic simulation is carried out on a local zone (for example a RVE) from the results of the macro-meso embedded simulations. The deformed configuration obtained by the embedded mesoscopic simulation constitutes the initial state of the local mesoscopic calculation.This configuration has some drawbacks, in particular excessive yarn elongations, but nevertheless it constitutes an initial state close to the solution and interesting for the local mesoscopic simulation.

4.2.1 Mesoscopic simulation

A hyperelastic transverse isotropic (Neo-Hookean) constitutive law is used to describe the mechanical behaviors of yarns. The strain energy potential is divided into two parts [65]:

$$w = w_{iso}(I_1, I_2, I_3) + w_{trans}(I_1, I_2, I_3, I_4, I_5) \tag{14}$$

The isotropic potential w_{iso} describes the longitudinal behaviour of a yarn, and the potential w_{trans} corresponds to the deformations of a yarn in the transverse plane. Table B2 in *Appendix B* shows the four material parameters used in the mesoscopic simulation [66]. This hyperelastic law is implemented in Abaqus/Explicit, by a VUMAT user subroutine. Contact with friction between yarns is controlled by a penalty method and a Coulomb friction model with a coefficient of 0.21 [64].

4.2.2 Three points bending: local mesoscopic simulation

The local mesoscopic simulation must be linked to the macroscopic simulation. In the case of three-point bending, the displacements of all nodes of the meso embedded analysis are relaxed except for the nodes of the right and left sections of the RVE for which the components of displacement in the direction of the beam are set equal to those of the macroscopic calculation. The results of the extensions obtained by the embedded mesoscopic analysis and by the local mesoscopic analysis are shown in Fig.20.

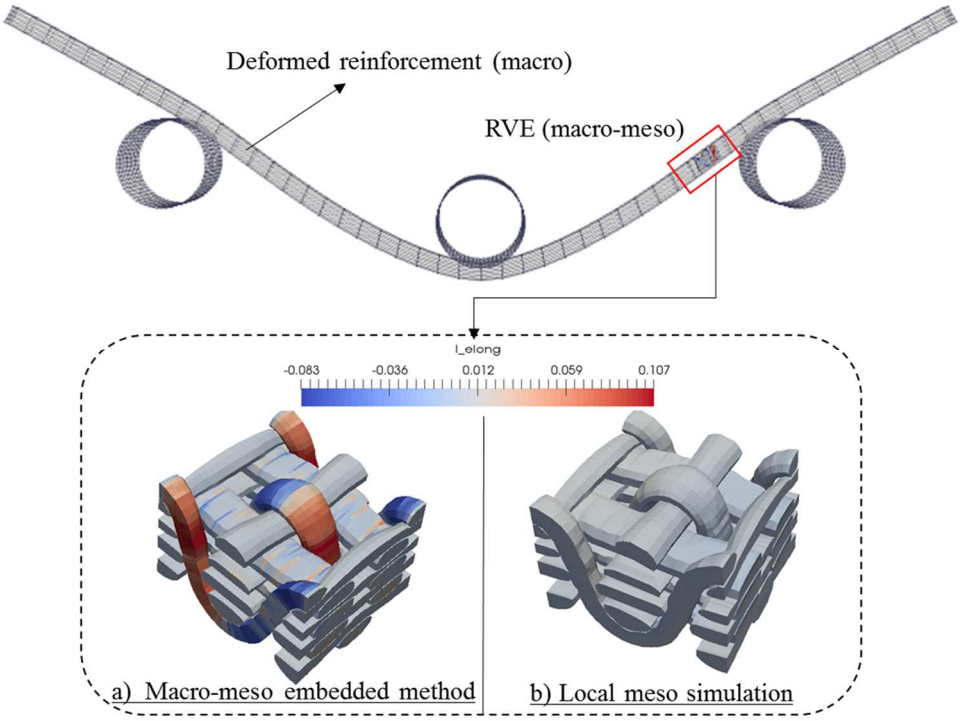

Fig. 20. Three points bending: mesoscopic simulations of a RVE. a) Elongation in macro-meso embedded analysis b) Elongation in local mesoscopic simulation analysis

The elongation of ten elements located in different areas of this RVE are displayed in Fig.21. This shows that the spurious elongations obtained in the macro-meso embedded analysis are mostly removed by the local mesoscopic simulation.

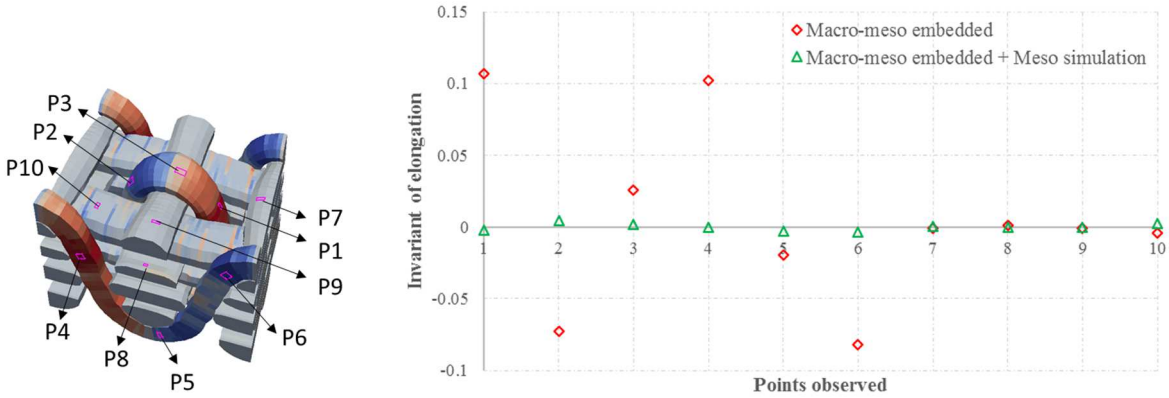

Fig.21 Elongation at different points obtained by the macro-meso embedded analysis and the local mesoscopic simulation in a RVE of the reinforcement in three points bending

4.2.3 Hemispherical forming: local mesoscopic simulation

During hemispherical stamping, in-plane shear is the main deformation mode because it is necessary to obtain the spherical geometry which is double curved. A RVE in the high-shear zone is analyzed (Fig.22). A macro-meso embedded analysis of the entire textile reinforcement is first carried out. It leads to spurious elongations of the yarns (Fig. 22a). In the local mesoscopic calculation, all the displacements of the macro-meso embedded analysis inside the cell are relaxed. On the edges, the displacements in the plane of the cell are retained for the yarns oriented by the edge. For the other yarns the displacements in the cell plane are retained in the center of the yarn. Relative slippage between the yarns in contact is possible. The comparison before and after this simulation (Fig. 22) shows the excessive elongation phenomenon have been avoided. Because this RVE is subjected to a high shear stress, the sections of the ends of yarns no longer remain parallel with the yarns in the other direction.

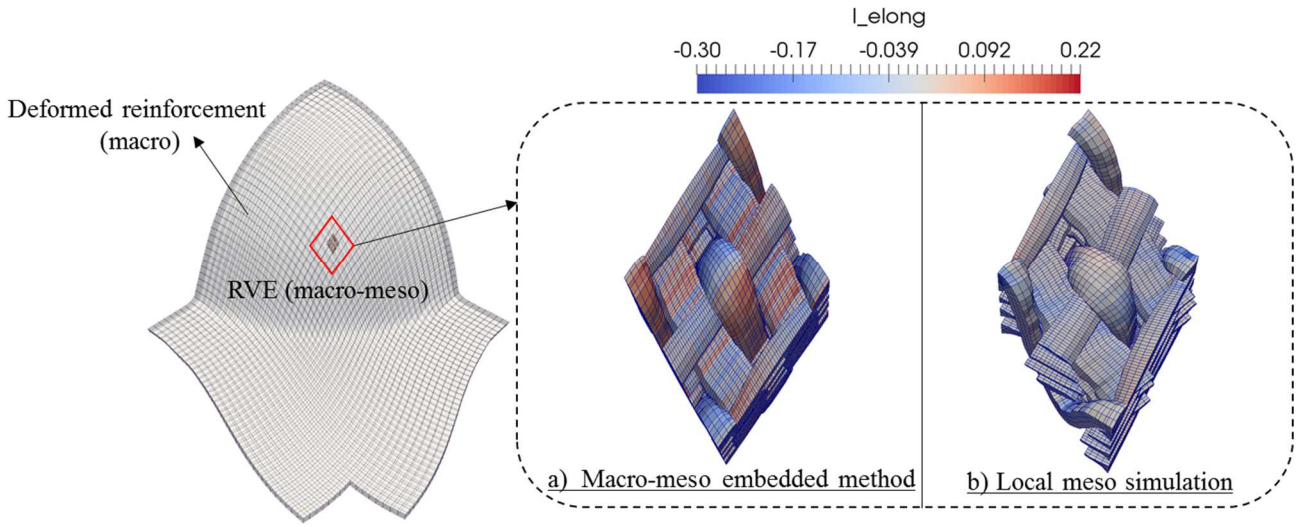

Fig.22 Hemispherical stamping: mesoscopic simulations of a RVE. a) Elongation in macro-meso embedded analysis b) Elongation in local mesoscopic simulation analysis

The elongation of ten elements located in different areas of this RVE are display in Fig 23. This shows that the spurious elongations obtained in the macro-meso embedded analysis are avoided by the local mesoscopic simulation.

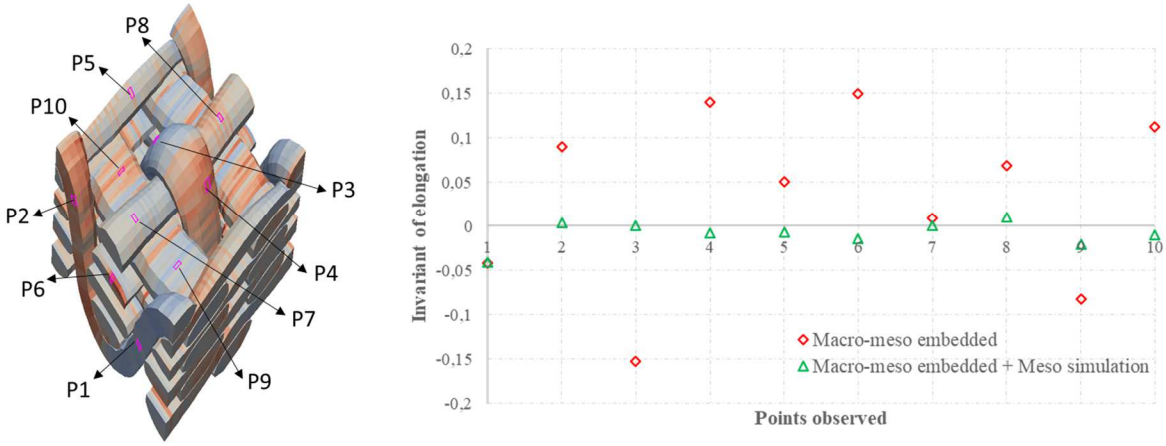

Fig.23. Elongation at different points obtained by the macro-meso embedded analysis and the local mesoscopic simulation in a RVE in hemispherical stamping

4.3 Comparisons of numerical and experimental results at the mesoscale

To demonstrate the correctness of the proposed approach, the numerical and experimental results are compared in the case of three points bending. The bending experiment is performed under the same condition as described in section 2.5.1. After the bending, a resin is injected into the deformed fabric. Then, the fabric fixed by the resin is cut on the section of binder yarn. This makes it possible to observe the deformed geometry of the yarns (Fig.24).

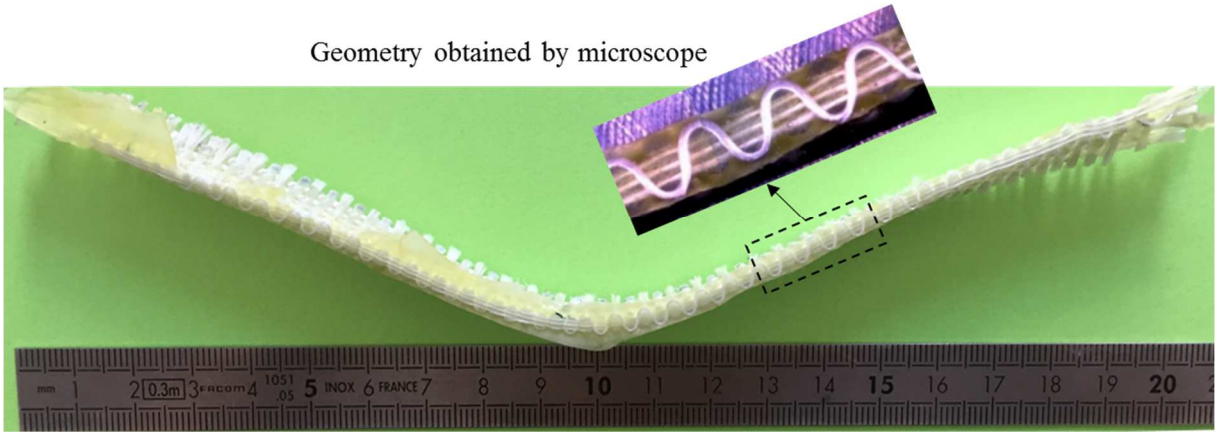

Fig. 24. Observation of mesoscopic geometry of the deformed reinforcement by microscope

A comparison between the experimental and simulated geometry of a deformed RVE is presented in Fig. 25. They are in good agreement. In both cases, slippage occurs between the yarns during the bending deformation of the reinforcement.

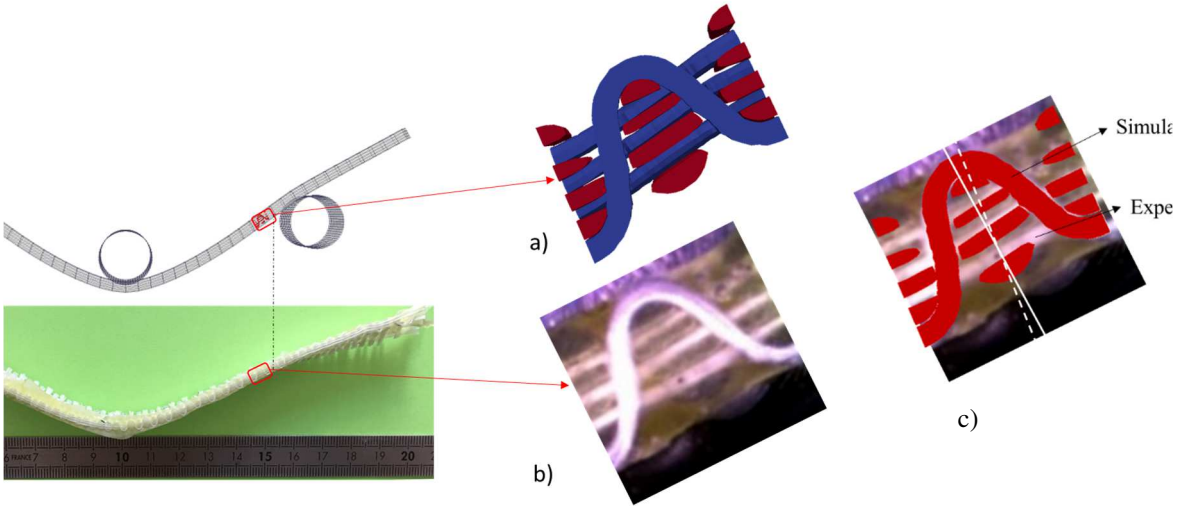

Fig. 25. Woven unit cells in the same position obtained by:
a) Local mesoscopique simulation b) experiment c) comparison

5. Conclusion

Analyses on a mesoscopic scale give the internal geometry and therefore the deformations and internal defects of textile reinforcements during forming. Draping of woven fabrics can be simulated by mesoscopic analysis of the entire preform, but these simulations lead to generally prohibitive computation times. An approach based on the macroscopic simulation of the forming process and the embedded mesoscopic model was presented. It provides a solution at the mesoscopic scale by a local analysis based on the embedded geometry. The local mesoscopic model is linked to the macroscopic model at its edges, but is relaxed enough to avoid spurious extensions. This local mesoscopic calculation is only carried out in areas where this analysis is necessary, e.g. maximum shear zones or regions of high curvature. It has been shown that the approach achieves the mesoscopic deformation of a woven cell in the case of three-point bending of the textile reinforcement and in the case of a hemispherical forming. In the latter case, local deformation of a sheared woven cell was obtained.

The deformed geometries obtained by the mesoscopic analysis can be used to determine the change in fibre volume fraction of the yarns during draping and their consequences on the mechanical properties of the cured composite. In addition, the voids obtained between the deformed yarns can change the permeability of the textile reinforcement.

The objective of this paper was to show the feasibility of this meso-macro approach. Validation work, determination of the precision will be a next step in particular by extending the comparisons to different cases of forming and different unit cells in the reinforcement.

Declaration of Competing Interest

The authors declare that they have no known competing financial interests or personal relationships that could have appeared to influence the work reported in this paper.

Acknowledgment

This work was supported by the ANR, (French Research Agency), grant aap-rmnp-2013-INTERLOCK and by the China Scholarship Council (CSC) (J. Wang).

Appendix A. Material parameters of the studied reinforcement

Table A1. Material parameters used for macroscopic simulations (k_i in MPa, D_0 in Nmm, D_1 in Nmm2)

$W_{elong1/2}$	k_1	k_2	k_3	k_4	k_5	k_6
	8.692	4.816e3	-1.002e6	8.275e7	-2.419e9	2.442e10
	k_7	k_8	k_9	k_{10}	k_{11}	k_{12}
	8.692	-5.056e2	1.073e5	-2.687e6	0	0
W_{comp}	k_1/ k_7	k_2/ k_8	k_3/ k_9	k_4/ k_{10}	k_5/ k_{11}	k_6/ k_{12}
	9.69e-2	7.009e-1	6.426e-2	-1.339e0	8.777e-1	2.855e-2
W_{sh}	k_1/ k_7	k_2/ k_8	k_3/ k_9	k_4/ k_{10}	k_5/ k_{11}	k_6/ k_{12}
	3.441e-1	-2.019e0	7.416e0	-1.401e1	1.401e1	-5.444e0
W_{shT1}	k_1/ k_7	k_2/ k_8	k_3/ k_9	k_4/ k_{10}	k_5/ k_{11}	k_6/ k_{12}
	3.721e-2	3.844e-2	-5.21e-1	1.877e0	-2.78e0	1.572e0
W_{shT2}	k_1/ k_7	k_2/ k_8	k_3/ k_9	k_4/ k_{10}	k_5/ k_{11}	k_6/ k_{12}
	3.473e2	-5.674e-2	-1.46e-2	5.835e-1	-1.201e0	8.084e-1
		D_0 (warp)	D_1 (warp)	D_0 (weft)	D_1 (weft)	
		3.6	117.9	3.748	123.6	

Appendix B. Hyperelastic transverse isotropic constitutive law for the mesoscopic simulation

The hyperelastic transverse isotropic (Neo-Hookean) constitutive law is made up of a sum of two potentials [65]: the isotropic potential w_{iso} describes the longitudinal behaviour of a yarn, and the potential w_{trans} corresponds to the deformations of a yarn in the transverse plane.

$$\begin{cases} w = w_{iso}(I_1, I_2, I_3) + w_{trans}(I_1, I_2, I_3, I_4, I_5) \\ w_{iso} = \frac{1}{2}\mu(I_1 - 3) - \mu\ln(J) + \frac{1}{2}\lambda(J-1)^2 \\ w_{trans} = \left[\alpha + \beta\ln(J) + \gamma(I_4 - 1)\right](I_4 - 1) - \frac{1}{2}\alpha(I_5 - 1) \end{cases} \quad \text{(B1)}$$

The parameters λ, μ, α, β and γ are defined in Equation (B2) according to the four material parameters: transverse modulus of elasticity E, longitudinal modulus of elasticity E_A, Poisson's ratio ν and longitudinal shear modulus G_A. Then the material parameters used in the mesoscopic simulation are given in Table B2 [66].

Table B2. Material parameters used in Neo-Hookean constitutive law

E (MPa)	E_A (MPa) elongation	E_A (MPa) compression	ν	G_A (MPa)
3200	45516	100	0	1600

$$\lambda = \frac{E(\nu + n\nu^2)}{m(1+\nu)} \quad \mu = \frac{E}{2(1+\nu)} \quad \alpha = \mu - G_A \quad \beta = \frac{E\nu^2(1-n)}{4m(1+\nu)} \quad \gamma = \frac{E_A(1-\nu)}{8m} - \frac{\lambda + 2\mu}{8} + \frac{\alpha}{2} - \beta$$
$$m = 1 - \nu - 2n\nu^2 \quad n = E_A / E \quad \text{(B2)}$$

References

[1] Gereke, T., Döbrich, O., Hübner, M., & Cherif, C. (2013). Experimental and computational composite textile reinforcement forming: A review. Composites Part A: Applied Science and Manufacturing, 46, 1-10.

[2] Bussetta, P., & Correia, N. (2018). Numerical forming of continuous fibre reinforced composite material: A review. Composites Part A: Applied Science and Manufacturing, 113, 12-31.

[3] Skordos, A. A., Aceves, C. M., & Sutcliffe, M. P. (2007). A simplified rate dependent model of forming and wrinkling of pre-impregnated woven composites. Composites Part A: Applied science and manufacturing, 38(5), 1318-1330.

[4] Boisse, P., Hamila, N., Vidal-Sallé, E., & Dumont, F. (2011). Simulation of wrinkling during textile composite reinforcement forming. Influence of tensile, in-plane shear and bending stiffnesses. Composites Science and Technology, 71(5), 683-692.

[5] Dangora, L. M., Mitchell, C. J., & Sherwood, J. A. (2015). Predictive model for the detection of out-of-plane defects formed during textile-composite manufacture. Composites Part A: Applied Science and Manufacturing, 78, 102-112.

[6] Sjölander, J., Hallander, P., & Åkermo, M. (2016). Forming induced wrinkling of composite laminates: a numerical study on wrinkling mechanisms. Composites Part A: applied science and manufacturing, 81, 41-51.

[7] Gatouillat, S., Bareggi, A., Vidal-Sallé, E., & Boisse, P. (2013). Meso modelling for composite preform shaping–simulation of the loss of cohesion of the woven fibre network. Composites Part A: Applied science and manufacturing, 54, 135-144.

[8] Allaoui, S., Hivet, G., Soulat, D., Wendling, A., Ouagne, P., & Chatel, S. (2014). Experimental preforming of highly double curved shapes with a case corner using an interlock reinforcement. International Journal of Material Forming, 7(2), 155-165.

[9] Schirmaier, F. J., Dörr, D., Henning, F., & Kärger, L. (2017). A macroscopic approach to simulate the forming behaviour of stitched unidirectional non-crimp fabrics (UD-NCF). Composites Part A: Applied Science and Manufacturing, 102, 322-335

[10] Schirmaier, F. J., Weidenmann, K. A., Kärger, L., & Henning, F. (2016). Characterisation of the draping behaviour of unidirectional non-crimp fabrics (UD-NCF). Composites Part A: Applied Science and Manufacturing, 80, 28-38.

[11] Tephany, C., Gillibert, J., Ouagne, P., Hivet, G., Allaoui, S., & Soulat, D. (2016). Development of an experimental bench to reproduce the tow buckling defect appearing during the complex shape forming of structural flax based woven composite reinforcements. Composites Part A: Applied Science and Manufacturing, 81, 22-33.

[12] Salem, M. M., De Luycker, E., Fazzini, M., & Ouagne, P. (2019). Experimental, analytical and numerical investigation to prevent the tow buckling defect during fabric forming. Composites Part A: Applied Science and Manufacturing, 125, 105567

[13] Bréard, J., Henzel, Y., Trochu, F., & Gauvin, R. (2003). Analysis of dynamic flows through porous media. Part I: Comparison between saturated and unsaturated flows in fibrous reinforcements. Polymer composites, 24(3), 391-408.

[14] Loix, F., Badel, P., Orgéas, L., Geindreau, C., & Boisse, P. (2008). Woven fabric permeability: From textile deformation to fluid flow mesoscale simulations. Composites science and Technology, 68(7-8), 1624-1630.

[15] Tran, T., Comas-Cardona, S., Abriak, N. E., & Binetruy, C. (2010). Unified microporomechanical approach for mechanical behavior and permeability of misaligned unidirectional fiber reinforcement. Composites Science and Technology, 70(9), 1410-1418.

[16] Gangloff Jr, J. J., Simacek, P., Sinha, S., & Advani, S. G. (2014). A process model for the compaction and saturation of partially impregnated thermoset prepreg tapes. Composites Part A: Applied Science and Manufacturing, 64, 234-244.

[17] Zeng, X., Endruweit, A., Brown, L. P., & Long, A. C. (2015). Numerical prediction of in-plane permeability for multilayer woven fabrics with manufacture-induced deformation. Composites Part A: Applied Science and Manufacturing, 77, 266-274.

[18] Whitcomb, J., Srirengan, K., & Chapman, C. (1995). Evaluation of homogenization for global/local stress analysis of textile composites. Composite structures, 31(2), 137-149.

[19] Carvelli, V., & Poggi, C. (2001). A homogenization procedure for the numerical analysis of woven fabric composites. Composites Part A: Applied Science and Manufacturing, 32(10), 1425-1432.

[20] Lomov, S. V., Ivanov, D. S., Verpoest, I., Zako, M., Kurashiki, T., Nakai, H., & Hirosawa, S. (2007). Meso-FE modelling of textile composites: Road map, data flow and algorithms. Composites Science and Technology, 67(9), 1870-1891.

[21] Obert, E., Daghia, F., Ladevèze, P., & Ballere, L. (2014). Micro and meso modeling of woven composites: Transverse cracking kinetics and homogenization. Composite Structures, 117, 212-221.

[22] El Said, B., & Hallett, S. R. (2018). Multiscale surrogate modelling of the elastic response of thick composite structures with embedded defects and features. Composite Structures, 200, 781-798.

[23] Liang, B., Zhang, W., Fenner, J. S., Gao, J., Shi, Y., Zeng, D., ... & Cao, J. (2019). Multi-scale modeling of mechanical behavior of cured woven textile composites accounting for the influence of yarn angle variation. Composites Part A: Applied Science and Manufacturing, 124, 105460.

[24] Creech, G., & Pickett, A. K. (2006). Meso-modelling of non-crimp fabric composites for coupled drape and failure analysis. Journal of materials science, 41(20), 6725-6736.

[25] Pickett, A. K., Sirtautas, J., & Erber, A. (2009). Braiding simulation and prediction of mechanical properties. Applied Composite Materials, 16(6), 345.

[26] Bayraktar, H., Ehrlich, D., Scarat, G., McClain, M., Timoshchuk, N., & Redman, C. (2015). Forming and performance analysis of a 3D-woven composite curved beam using meso-scale FEA. Sampe Journal, 51(3), 23.

[27] Daelemans, L., Faes, J., Allaoui, S., Hivet, G., Dierick, M., Van Hoorebeke, L., & Van Paepegem, W. (2016). Finite element simulation of the woven geometry and mechanical behaviour of a 3D woven dry fabric under tensile and shear loading using the digital element method. Composites Science and Technology, 137, 177-187

[28] Thompson, A. J., El Said, B., Belnoue, J. P., & Hallett, S. R. (2018). Modelling process induced deformations in 0/90 non-crimp fabrics at the meso-scale. Composites Science and Technology, 168, 104-110.

[29] Iwata, A., Inoue, T., Naouar, N., Boisse, P., & Lomov, S. V. (2019). Coupled meso-macro simulation of woven fabric local deformation during draping. Composites Part A: Applied Science and Manufacturing, 118, 267-280.

[30] Whitcomb, J. D. (1991). Iterative global/local finite element analysis. Computers & structures, 40(4), 1027-1031.

[31] Dureisseix, D., & Farhat, C. (2001). A numerically scalable domain decomposition method for the solution of frictionless contact problems. International Journal for Numerical Methods in Engineering, 50(12), 2643-2666.

[32] Dhia, H. B., & Rateau, G. (2005). The Arlequin method as a flexible engineering design tool. International journal for numerical methods in engineering, 62(11), 1442-1462.

[33] Amini, A. M., Dureisseix, D., & Cartraud, P. (2009). Multi-scale domain decomposition method for large-scale structural analysis with a zooming technique: Application to plate assembly. International Journal for Numerical Methods in Engineering, 79(4), 417-443.

[34] Gendre, L., Allix, O., & Gosselet, P. (2011). A two-scale approximation of the Schur complement and its use for non-intrusive coupling. International Journal for Numerical Methods in Engineering, 87(9), 889-905.

[35] LLorca, J., González, C., Molina-Aldareguía, J. M., Segurado, J., Seltzer, R., Sket, F., ... & Canal, L. P. (2011). Multiscale modeling of composite materials: a roadmap towards virtual testing. Advanced Materials, 23(44), 5130-5147.

[36] Criscione, J. C., Douglas, A. S., & Hunter, W. C. (2001). Physically based strain invariant set for materials exhibiting transversely isotropic behavior. Journal of the Mechanics and Physics of Solids, 49(4), 871-897.

[37] Itskov, M., & Aksel, N. (2004). A class of orthotropic and transversely isotropic hyperelastic constitutive models based on a polyconvex strain energy function. International journal of solids and structures, 41(14), 3833-3848.

[38] Balzani, D., Neff, P., Schröder, J., & Holzapfel, G. A. (2006). A polyconvex framework for soft biological tissues. Adjustment to experimental data. International journal of solids and structures, 43(20), 6052-6070.

[39] Ten Thije, R. H. W., Akkerman, R., & Huétink, J. (2007). Large deformation simulation of anisotropic material using an updated Lagrangian finite element method. Computer methods in applied mechanics and engineering, 196(33-34), 3141-3150.

[40] Aimène, Y., Vidal-Sallé, E., Hagège, B., Sidoroff, F., & Boisse, P. (2010). A hyperelastic approach for composite reinforcement large deformation analysis. Journal of Composite materials, 44(1), 5-26.

[41] Charmetant, A., Orliac, J. G., Vidal-Sallé, E., & Boisse, P. (2012). Hyperelastic model for large deformation analyses of 3D interlock composite preforms. Composites Science and Technology, 72(12), 1352-1360.

[42] Boisse, P., Hamila, N., & Madeo, A. (2018). The difficulties in modeling the mechanical behavior of textile composite reinforcements with standard continuum mechanics of Cauchy. Some possible remedies. International Journal of Solids and Structures, 154, 55-65.

[43] Mathieu, S., Hamila, N., Bouillon, F., & Boisse, P. (2015). Enhanced modeling of 3D composite preform deformations taking into account local fiber bending stiffness. Composites Science and Technology, 117, 322-333

[44] Dell'Isola, F., & Steigmann, D. (2015). A two-dimensional gradient-elasticity theory for woven fabrics. Journal of Elasticity, 118(1), 113-125.

[45] Madeo, A., Ferretti, M., Dell'Isola, F., & Boisse, P. (2015). Thick fibrous composite reinforcements behave as special second-gradient materials: three-point bending of 3D interlocks. Zeitschrift für angewandte Mathematik und Physik, 66(4), 2041-2060.

[46] d'Agostino, M. V., Giorgio, I., Greco, L., Madeo, A., & Boisse, P. (2015). Continuum and discrete models for structures including (quasi-) inextensible elasticae with a view to the design and modeling of composite reinforcements. International Journal of Solids and Structures, 59, 1-17.

[47] Vilfayeau J. Modélisation numérique du procédé de tissage des renforts fibreux pour matériaux composites. PhD Thesis, INSA Lyon, France 2014

[48] Boehler, J. P. (1987). Applications of tensor functions in solid mechanics (Vol. 292). J. P. Boehler (Ed.). New York: Springer.

[49] Mitchell, C., Dangora, L., Bielmeier, C., & Sherwood, J. (2016). Investigation into the changes in bending stiffness of a textile reinforced composite due to in-plane fabric shear: Part 2–Numerical analysis. Composites Part A: Applied Science and Manufacturing, 85, 138-147.

[50] Yao, Y., Peng, X., & Gong, Y. (2019). Influence of tension–shear coupling on draping of plain weave fabrics. Journal of materials science, 54(8), 6310-6322.

[51] Alshahrani, H. (2020). Characterization and finite element modeling of coupled properties during polymer composites forming processes. Mechanics of Materials, 103370.

[52] Onate, E., & Zárate, F. (2000). Rotation-free triangular plate and shell elements. International Journal for Numerical Methods in Engineering, 47(1-3), 557-603.

[53] Lebrun, G., Bureau, M.N., Denault, J., (2003). Evaluation of bias-extension and picture-frame test methods for the measurement of intraply shear properties of PP/glass commingled fabrics. Composite Structures 61, 341–352.

[54] Cao, J., Akkerman, R., Boisse, P., Chen, J., Cheng, H. S., De Graaf, E. F., ... & Lee, W. (2008). Characterization of mechanical behavior of woven fabrics: experimental methods and benchmark results. Composites Part A: Applied Science and Manufacturing, 39(6), 1037-1053.

[55] Na, W., Ahn, H., Han, S., Harrison, P., Park, J. K., Jeong, E., & Yu, W. R. (2016). Shear behavior of a shear thickening fluid-impregnated aramid fabrics at high shear rate. Composites Part B: Engineering, 97, 162-175.

[56] Boisse, P., Hamila, N., Guzman-Maldonado, E., Madeo, A., Hivet, G., & Dell'Isola, F. (2017). The bias-extension test for the analysis of in-plane shear properties of textile composite reinforcements and prepregs: a review. International Journal of Material Forming, 10(4), 473-492.

[57] Software PLASFIB, Paris, Inter Deposit Certification, agence pour la protection des programmes. 2011 and 2015.

[58] Hamila, N., & Boisse, P. (2007). A meso–macro three node finite element for draping of textile composite preforms. Applied composite materials, 14(4), 235-250.

[59] Hamila, N., Boisse, P., Sabourin, F., & Brunet, M. (2009). A semi-discrete shell finite element for textile composite reinforcement forming simulation. International journal for numerical methods in engineering, 79(12), 1443-1466.

[60] Miehe, C., & Dettmar, J. (2004). A framework for micro–macro transitions in periodic particle aggregates of granular materials. Computer Methods in Applied Mechanics and Engineering, 193(3-5), 225-256.

[61] Naouar, N., Vidal-Salle, E., Schneider, J., Maire, E., & Boisse, P. (2015). 3D composite reinforcement meso FE analyses based on X-ray computed tomography. Composite Structures, 132, 1094-1104.

[62] Long, A. C., & Brown, L. P. (2011). Modelling the geometry of textile reinforcements for composites: TexGen. In Composite reinforcements for optimum performance (pp. 239-264). Woodhead Publishing.

[63] Charmetant, A., Vidal-Sallé, E., & Boisse, P. (2011). Hyperelastic modelling for mesoscopic analyses of composite reinforcements. Composites Science and Technology, 71(14), 1623-1631.

[64] Hivet, G., Allaoui, S., Cam, B. T., Ouagne, P., & Soulat, D. (2012). Design and potentiality of an apparatus for measuring yarn/yarn and fabric/fabric friction. *Experimental mechanics*, *52*(8), 1123-1136.

[65] Bonet, J., & Burton, A. J. (1998). A simple orthotropic, transversely isotropic hyperelastic constitutive equation for large strain computations. Computer methods in applied mechanics and engineering, 162(1-4), 151-164.

[66] Florimond C. Contribution à la modélisation mécanique du comportement de mèches de renforts tissés à l'aide d'un schéma éléments finis implicite. PhD Thesis, INSA Lyon, France 2015